Reconstructing the Fluid–Structure Interaction of an Earthquake-Triggered LP-Gas Deflagration and Progressive Collapse in a Two-Storey Shopping Mall in Kumamoto, Japan, on 28 July 2026

Jun Ishimoto

Institute of Fluid Science, Tohoku University, 2-1-1 Katahira, Aoba-ku, Sendai 980-8577, Japan

Corresponding author: ishimoto@alba.ifs.tohoku.ac.jp — ORCID iD: 0000-0002-5674-643X

Preprint, 5 August 2026

Abstract

On 28 July 2026, approximately 80 minutes after the Mj 7.1 Kumamoto earthquake (maximum JMA seismic intensity 7), a large gas explosion destroyed part of a two-storey steel-frame shopping mall in Kashima Town, Kumamoto, Japan. Seven fatalities had been reported as of 30 July 2026. Public reporting indicates that the earthquake damaged the supply piping from an outdoor bulk LP-gas vessel and that leaked propane accumulated in a second-floor retail zone before igniting. This paper reconstructs the event using a three-stage fluid–structure interaction (FSI) chain built entirely from open-source tools: (i) a 3-D premixed-deflagration CFD model of an approximately 330 kg stratified propane cloud in a 160 m section of the mall (constructed with OpenFOAM XiFoam using Weller b–Xi flame-wrinkling closure and k–omega SST) ; (ii) a quasi-two-way venting FSI scheme in which 255 breakable envelope and floor panels are monitored during the run and opened through a deterministic mesh-rebuild restart when their failure pressure is exceeded, with capacities derived from Japanese design references and degraded by an earthquake damage factor; and (iii) an event-driven progressive-collapse and debris/dust dynamics model that distinguishes a column-first storey-crush (pancake) core from a hinge-type slab-unzipping periphery. The effective turbulent burning velocity is calibrated using two observables: the contiguous facade-stripping extent and the near-frame-one envelope failure, which are therefore calibration targets rather than validation metrics. With that single calibration, the reconstruction independently reproduces the absence of a sustained external fireball, the radial debris scatter on the tank-side facade, the localized roof breach above the ignition zone, the mixed crush/draped collapse morphology, and a dust-front speed of 8.8 m/s against a measured 13 m/s (band 8–17 m/s). The debris model is further tested, without any adjustment, against the ballistics recorded in the footage: it reproduces the observed launch-speed/apex pair, and the back-calculated impulse duration of 22 ms agrees with the 25 ms assumed a priori. However, it does not reproduce the longest observed throw distances, a deficiency reported here rather than removed by tuning. A uniform 0.5 m grid-refinement study shows that the facade-stripping extent and the sustained compartment overpressure are essentially unchanged, while the near-kernel peak, the external blast spike, and the local failure counts are not convergent and are reported with that caveat. An ignition-location sensitivity run, in which the kernel is moved to the back-of-house corridor position suggested by post-event drone imagery, leaves the headline conclusions — south-side damage concentration, a roof breach above the epicentre, and few-kilopascal interior loads acting on seismically weakened members — unchanged. A numerical pitfall is that the subsetMesh utility of OpenFOAM-v2606 assigns the constraint type "empty" to newly exposed patches, which silently turns off momentum solution on 3-D meshes. All findings are hypotheses for the official investigation and imply no attribution of responsibility. On the grounds of damage magnitude, impulse, and debris velocity, the reconstruction supports a fast deflagration rather than a cloud detonation, while a transient, localized transition cannot be excluded.

Keywords: gas explosion; vented deflagration; vapor cloud explosion; Natech; fluid–structure interaction; progressive collapse; CFD; forensic engineering; OpenFOAM; earthquake-triggered accident; LP gas; combustion regime; deflagration-to-detonation transition

1. Introduction

Earthquake-triggered gas releases are a recognized cascading hazard (Natech): ground shaking damages fuel-gas infrastructure, and delayed ignition of the accumulated cloud can produce structural damage far exceeding that of the shaking itself. The catastrophic explosion at a shopping mall in Kumamoto Prefecture on 28 July 2026 is a severe example: dashcam recordings carry an on-screen timestamp of 17:46 for the explosion (a device clock reading not independently calibrated), about 80 minutes after the mainshock, and the operator's public release reports the blast location as "the rear of the second floor". Aerial footage shows roughly 55 m of the front facade stripped to the frame, a local roof breach, and a partial collapse of the second floor in which floor plates dropped between largely standing columns, with a heavily crushed core zone.

Forensic reconstructions of building gas explosions have historically informed both regulation and structural engineering, from the Ronan Point town-gas explosion of 1968 [9] to modern vented-deflagration test programs [6] and code provisions for internal explosions [8]. Computational reconstructions, however, rarely close the gap between the gas-dynamic loading and the progressive structural failure that governs both the venting history and the final damage state: the opening of windows, cladding, and floor plates feeds back strongly on the achievable overpressure.

This study contributes: (1) quantitative evidence extracted from public video (the cloud kinematics, debris ballistics, damage extents, and timeline); (2) an open-source, reproducible three-stage fluid–structure interaction (FSI) chain coupling a premixed deflagration solver to a panel-resolved venting model with seismically degraded capacities, and to an event-driven progressive-collapse model that reproduces both storey-crushing and slab-draping morphologies; (3) a comparison against observables that were *not* used for calibration — the dust-front kinematics, the absence of a sustained external fireball, the rear-facade debris scatter and, in particular, the debris ballistics, which test the fragment model without any parameter being fitted to the footage; (4) a grid-sensitivity study on a uniformly refined 0.5 m mesh that separates the conclusions that survive refinement from those which do not; and (5) documentation of the silent solver-crippling behaviour of a standard OpenFOAM mesh utility that is directly relevant to any explosion-venting workflow using cell-removal geometry. The reconstruction is based exclusively on public information; building dimensions and inventories are typified where unknown.

2. Incident Evidence from Public Sources

2.1 Timeline and mechanism as publicly reported

The mainshock occurred at 16:27 JST on 28 July 2026 with Mj 7.1 and a maximum seismic intensity of 7 [14], where Mj denotes the magnitude scale of the Japan Meteorological Agency (JMA), and the JMA seismic intensity is a closed scale running from 0 to 7 that is distinct from the Modified Mercalli scale. According to the operator's press release of 29 July, customers and staff were evacuated outdoors by about 17:00, and ceiling falls, partial exterior wall damage, and sprinkler releases were confirmed during the post-quake inspection. The explosion occurred at "the rear of the 2nd floor" at 17:50 as reported by the operator, while dashcam timestamps read 17:46:24 [15]. The two times differ by about four minutes. Because the dashcam clock is not independently calibrated and the operator's time may be a report-receipt time, no attempt is made here to resolve the discrepancy, and the accumulation interval is treated as approximately 80 minutes in either case. A television documentary aired on 3 August 2026 [15] reports, based on drone surveys of the site, the operator's statement that the explosion was "concentrated in one corner of the south side"; identifies a staff-only back-of-house corridor running behind the second-floor shops as the suspected accumulation space; and notes an expert assessment that rooftop cooling units directly above that corridor were thrown upward "by pressure from below", marking the estimated epicentre. The same programme also reports that a gas odour had been noticed inside the store before the explosion.

Broadcast commentary raised the question of whether seismic shutoff provisions on the bulk LP-gas installation operated as intended; this point is reportedly under official investigation and is not addressed by the present study [15]. What is used here as a modelling premise, and only as a premise, is the publicly reported outcome: that a sustained release from the damaged supply line accumulated in a second-floor fashion-retail zone (not a restaurant zone) over the interval between the mainshock and the explosion. As of 30 July 2026, seven fatalities had been reported; this figure was still subject to change at the time of writing.

2.2 Quantitative video analysis

Frame-by-frame analysis of two dashcam clips (30 fps) and extended aerial footage was performed using utility poles (with a visible height of 10.5–12.5 m) and vehicles as length references at the cloud distance; the absolute scale uncertainty is estimated at ±35–40%. Table 1 summarizes the observables used as reconstruction targets. Notably, the very first post-onset frame (33 ms) already shows a ~27 m-wide eruption above the roofline, indicating near-simultaneous envelope failure over tens of meters. It should be emphasized that this observation constrains the internal *pressure field* rather than the flame speed: pressure equalization within a compartment proceeds on the acoustic timescale (~340 m/s, i.e. well under 0.1 s across the cloud length), so the failure of panels tens of metres apart within a single frame does not require the flame front to have traversed that distance. No sustained fireball appears in any clip. A close-range recording aired on 3 August [15] shows only brief, localized orange luminosity at the base of the erupting cloud, lasting approximately one second; this is consistent with transient flame jets at the vent openings and with an inside-burning lean-to-stoichiometric LPG deflagration venting combustion products and entraining structural dust.

Table 1. Reconstruction targets and contextual evidence from public sources (the ±35–40% scale uncertainty applies to footage-derived lengths and speeds). The last three rows are contextual evidence used qualitatively in Sections 4.1 and 5, not simulation targets.

Observable	Value	Basis
Explosion onset	17:46:24 JST (dashcam clock); 17:50 (operator release)	timestamp overlay
Initial dust-front speed	13 m/s (range 8–17)	first 0–0.6 s, single-clip differencing
Late front speed	4 m/s (range 3–7)	t = 4–7 s
Roof-debris launch speed	30–40 m/s vertical; apex ~24 m (band 15–33 m)	ballistic fit, gravity-consistent (no slow-motion)
Facade fully stripped	~55 m contiguous (±15 m), stripped to the frame	aerial, parking-stall/vehicle scale

Observable	Value	Basis
Facade partially damaged	~95 m total	aerial
Roof breach	local, 10–15 m across, deck folded inward	aerial
Collapse morphology	floor plates dropped between standing columns; heavily crushed core	aerial close-ups
External fireball	no sustained fireball; brief base flashes in one close view	both angles, 0–14 s; 3 Aug broadcast close view [15]
Debris throw	steel sheeting to ~100 m (lower bound)	aerial
Vehicle damage	one truck driving past the mall wrecked by the blast; dashcams in the nearby queue recorded continuously	broadcast reports [15]
Rooftop equipment	cooling units above the epicentre thrown upward; roof holed (pre/post drone comparison)	drone survey, 3 Aug broadcast [15]
Estimated epicentre	2F back-of-house staff corridor, south edge	expert assessment based on drone imagery [15]

3. Reconstruction Method

3.1 Geometry and gas-accumulation scenario

A 160-m-long section of the two-storey steel-frame mall was modelled on an integer-metre lattice (Fig. 1) and consisted of a 10 m column grid, second floor at z = 6 m, roof deck at z = 11 m, parapet 12 m high, south tenant strip (30 m deep), 10 m central corridor, north strip containing a statically walled cinema box and food-court zone, and 1 × 1 × 2–3 m merchandising obstacles in the tenant strip (congestion). The baseline computational domain was 200 × 110 × 26 m, discretized with 1.0 m hexahedral cells (0.57 M cells). A uniformly refined 0.5 m mesh was used for the sensitivity study of Section 4.3. The stratified propane cloud occupied the tenant strip over 75 < x < 125 m, with fuel mass-fraction layers in the order 0.058 / 0.045 / 0.030 from floor to ceiling, corresponding to equivalence ratios of approximately 0.97, 0.74, and 0.48 for a stoichiometric propane mass fraction of 0.060 (near-stoichiometric to lean with a propane vapor density 1.55 times that of air). The cloud integrates to 325.5 kg on the 1.0 m grid and 331.0 kg on the 0.5 m grid — a 1.7% difference arising from cell-centre snapping at the z = 8.5 m layer boundary — and is quoted as approximately 330 kg throughout. This order of magnitude is consistent with tens of minutes of release from a damaged bulk-vessel supply line. Ignition was a 2.5 m spherical kernel at floor level in the cloud centre. The 80-minute accumulation itself was not simulated. The cloud was an initial condition, and its extent was a hypothesis.

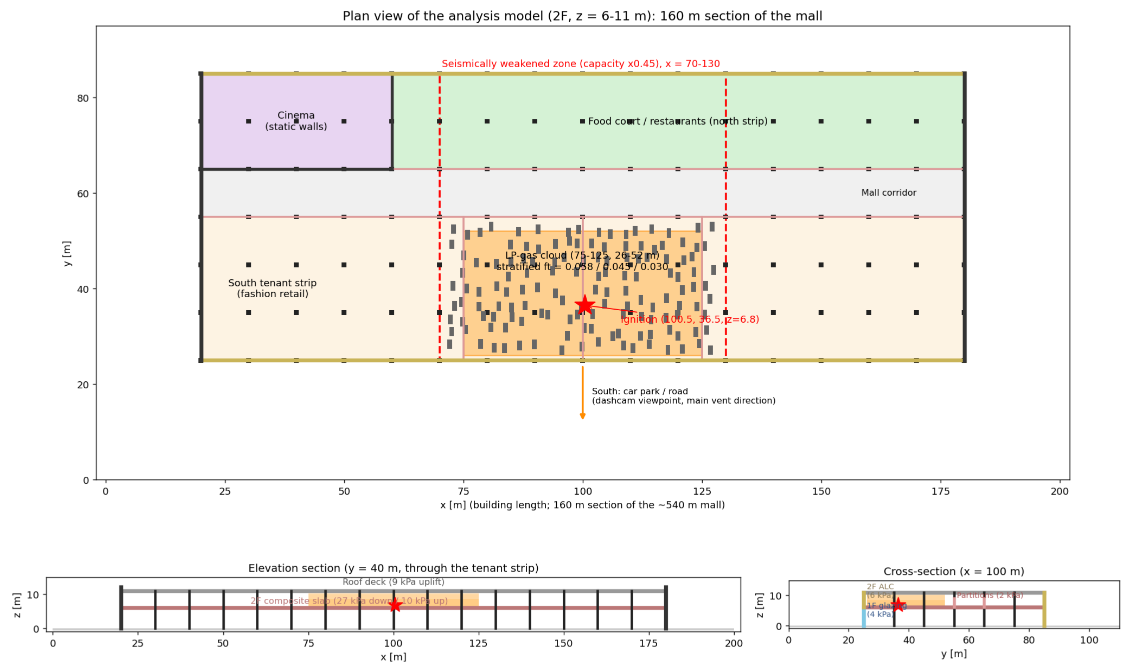

Figure 1. Analysis model: plan (top), elevation y = 40 m (bottom left), cross-section x = 100 m (bottom right). Orange: stratified LP-gas cloud; red dashes: seismically weakened zone (capacity × 0.45); star: ignition.

3.2 Deflagration CFD

The premixed deflagration was computed with the XiFoam solver of OpenFOAM-v2606 [4]. The computation used a Favre-averaged compressible flow, regression variable b with Weller flame-wrinkling closure [1], unstrained laminar flame speed from the Gülder correlation for propane [2], heheuPsiThermo two-state thermodynamics with an inhomogeneous fuel/oxidant/product mixture with JANAF C3H8 properties and a mixture fraction capped just below stoichiometric to remain within the model's lean-side validity, and the k–omega shear-stress transport (SST) turbulence model [3] (k–epsilon was found to be non-robust for impulsive venting jets at this resolution, with runaway turbulent viscosity). The boundary conditions were a wave-transmissive far field and wall functions on all solid surfaces. The time step was limited to 0.25 ms on the baseline grid (with an acoustic Courant–Friedrichs–Lewy number of ~0.09) and to 0.125 ms on the refined grid.

At 1 m resolution, a Reynolds-averaged Navier–Stokes (RANS) model cannot spontaneously reproduce the obstacle-driven flame acceleration observed in a congested retail interior. Following the established practice of congestion-calibrated effective burning velocities in industrial VCE tools [6, 13], the wrinkling factor was prescribed as Xi = 50. Because the cloud is stratified, the unstrained laminar flame speed S_L differs between layers, so the effective turbulent burning velocity S_T = Xi x S_L is not a single value: it ranges from approximately 8 m/s in the lean ceiling layer (ft = 0.030) to approximately 20 m/s in the near-stoichiometric floor layer (ft = 0.058), spanning the 4–20 m/s range reported for highly congested spaces.

This wrinkling factor is the single significant calibration parameter of the gas-dynamic stage. It was selected to reproduce two observables — the contiguous facade-stripping extent and the near-frame-one envelope failure. Those two quantities are consequently **calibration targets rather than independent validations,** and they are labelled as such in Table 5. Prescribed (assumed but not calibrated) parameters of the collapse and debris stage are listed separately in Table 3, so that the reader can distinguish computed quantities from modelling choices throughout.

3.3 Vent-panel FSI (quasi-two-way coupling)

The building envelope and floors were decomposed into 255 failure panels (Table 2), each embedded in the mesh as a zero-thickness baffle. During the run, the pressure difference across each panel was monitored with probe pairs. When the two most recent samples exceeded the panel capacity, the run was checkpointed, and the panel was opened. The opening was implemented with a deterministic mesh rebuild (blockMesh → removal of obstacles/columns from the cells · baffle creation for the surviving panels only). The cell ordering of this pipeline was verified to be bit-reproducible: the maximum cell-centre displacement between rebuilds was less than 1e−13 m on the 1.0 m grid and 8.5e−14 m on the 0.5 m grid. Consequently, the volume fields were carried over unchanged, and only face-based fluxes were re-initialized. Venting therefore feeds back on the interior pressure, with a resolution of 1 leg at 10–20 ms. Capacities followed Japanese design references (glazing, ALC rocking-clip connections, LGS gypsum partitions, composite-deck slabs, AIJ composite-structure studs, and puddle-weld capacities [10]). Inside the blast zone, they were reduced by a factor of η = 0.45, which is within the damage-class-III residual-capacity range of the Japanese post-earthquake damage-classification standard [11] and consistent with the operator-reported pre-explosion ceiling/wall damage.

Table 2. Vent-panel classes and differential-pressure capacities (Δp) for each panel. Derivations are from JIS/AIJ-based section analysis.

Panel class	Unit size	Failure Δp (intact)	Failure Δp (η = 0.45 zone)
1F storefront glazing	10 × 6 m	4 kPa	1.8 kPa
ALC/metal facade (both	10 × 5–6	6 kPa	2.7 kPa

Panel class	Unit size	Failure Δp (intact)	Failure Δp (η = 0.45 zone)
storeys)	m		
Gypsum/LGS partitions	10 × 3 m	2 kPa	0.9 kPa
Roof deck tiles (uplift)	10 × 15 m	9 kPa	4.05 kPa
2F composite slab tiles (down/up)	10 × 10 m	27 / 10 kPa	12.2 / 4.5 kPa

3.4 Progressive collapse and debris/dust dynamics

The third stage converted the CFD failure record into building-destruction kinematics, resulting in 1,358 rigid fragments. CFD-failed panels fragmented and flew with an impulse v0 = min(|Δp|, 40 kPa) × 25 ms × A/m (capped at 55 m/s) and were advected by the time-resolved CFD velocity field with quadratic drag (with a drag coefficient of 1.2). In the fragment model, the roof tiles lumped the deck together with rooftop equipment and were assigned an areal density of 50 kg m^{-2}, whereas the debris identifiable in the aerial footage was steel skin roughly 0.8 mm thick, corresponding to an areal density of approximately 6.3 kg m^{-2}. The two classes were therefore kept distinct in the ballistic comparison of Section 4.2, where the identical impulse law was applied to sheeting of the lower areal density released from the same failed tiles.

Structural collapse was modelled event-wise with two mechanisms reflecting the observed morphology. The first was a storey-crush (pancake) core at x = 90–110 m, where blast impulse plus seismic degradation caused the columns to fail first (t = 0.35–0.7 s): each column split at the knee, the lower segment buckled outward, and the bays above — second-floor slab and roof tiles — dropped near-horizontally as units, stacking at rubble heights of ~1 m (slab) and ~2.2 m (roof). The second was a peripheral unzipping band within the weakened zone where support loss propagated tile-to-tile (0.35–0.65 s per tile), with each tile hinge-rotating about its last supported edge before detaching. These floor plates were draped between standing columns. Columns that lost three or more adjacent slab tiles subsequently toppled. Ground impacts of heavy fragments released dust bursts. These bursts consisted of 260,000 particles of dust advected by the CFD velocity field (which faded within 0.5 s after the 1.5 s CFD record ended), with settling and stochastic dispersion. Rendering used ParaView in batch mode.

The quantities in Table 3 are prescribed modelling choices rather than results. They are stated explicitly because they govern the timing and visual character of the collapse. They did not enter the gas-dynamic solution of Section 3.2, which is one-way coupled to this stage. The first of them — the 25 ms impulse duration — was subsequently tested against the footage in Section 4.2 and was not adjusted there.

Table 3. Prescribed parameters of the collapse and debris/dust stage (assumed values, not calibrated against the video record).

Parameter	Value	Basis/status
Fragment impulse duration	25 ms	assumed a priori; independently tested in Section 4.2
Impulse pressure cap	40 kPa	assumed; limits the near-kernel transient
Fragment speed cap	55 m/s	assumed
Drag coefficient/drag law	1.2/quadratic	assumed
Areal density, roof-tile class	50 kg m^{-2}	deck plus lumped rooftop equipment
Areal density, sheet class	6.3 kg m^{-2}	0.8 mm steel skin matched to the debris visible in the footage
Column failure window (crush core)	0.35–0.7 s	prescribed to reproduce the observed crush morphology
Slab unzipping delay	0.35–0.65 s per tile	prescribed
Column toppling criterion	loss of ≥ 3 adjacent slab tiles	assumed
Rubble stack heights	~1 m (slab); ~2.2 m (roof)	assumed from plate thickness and bay area

3.5 Verification and a numerical pitfall

The chain was verified stepwise:

1. Sealed-volume combustion reached the theoretical constant-volume pressure ratio (~9).

2. A vented pilot enclosure reproduced the canonical vented-deflagration signature (a pressure rise during burning outpaced venting, peaking, and the negative phase) [5, 7].

3. The simulation software solids4foam [12] provided an independent linear-elastic solution for a 10 m composite-slab strip under the degraded failure load (16.2 kPa), yielding a peak bending stress of 34.7 MPa. This is approximately 14 times the cracked-RC tensile capacity, confirming that the tabulated connection-governed capacities, not gross-section strength, control (Fig. 6).

4. Shock/acoustic transmission through opened panels was verified in minimal cases.

5. The ballistic integrator was checked against the closed-form quadratic-drag rise height $h = (\mu/2k) \ln(1 + k v_0^2/\mu g)$, where $k = ½ \rho_{air} C_d$, with agreement within 0.15% for every fragment tested. Grid sensitivity is assessed in Section 4.3.

During this work, a silent failure mode of OpenFOAM-v2606 was isolated that practitioners of explosion-venting simulations should be aware of: subsetMesh assigns the constraint type “empty” (intended for 2-D cases) to the patch that receives newly exposed faces. On a 3-D mesh, the presence of empty faces corrupts the solution-direction detection, and the momentum equation is never solved: pressure then spreads only diffusively, velocities remain at the single-step value $u \approx -\Delta t \nabla p/\rho$, and unphysical static high-pressure domes persist in open air; checkMesh reports such meshes as healthy. The fix is to retype the exposed patch as a wall before use. The symptoms, diagnosis, and minimal reproduction are included in the archived dataset.

4. Results

Unless stated otherwise, the results of Sections 4.1 and 4.2 are those of the 1.0 m baseline grid. The corresponding 0.5-m-grid values and the sensitivity of each conclusion to refinement are given in Section 4.3.

4.1 Failure sequence and pressures

Table 4 lists the simulated sequence, while Fig. 2 shows representative frames and Fig. 3 the overpressure histories. The ignition kernel generates a local +34 kPa transient that fails the roof tile and slab tile directly above and below the kernel and the nearest partitions within 40 ms. As the flame expands at the prescribed S_T, the tenant strip sustains instantaneous overpressures of 2.7–4.6 kPa (with a mean of 2.24 kPa over 0.05–0.30 s), sufficient to strip the degraded ALC facade panel-by-panel along a 60 m contiguous run of the south facade centred on the cloud, and to cause ten roof tiles clustered above the cloud to fail. An external blast of ~+2.9 kPa reaches the dashcam side of the road. Burning completes in ~1.5 s, with 79 of 255 panels failing owing to direct pressure. The subsequent progressive collapse (Section 3.4) adds the storey-crush core (9 columns; ~12 crushed bays) and a 48-tile unzipping band, for a total collapse footprint of ~50 × 40 m.

Ignition-location sensitivity. After the model was frozen, the 3 August broadcast [15] placed the estimated epicentre in the back-of-house corridor along the south edge, rather than in the tenant-zone interior. To test whether the conclusions depend on the assumed ignition point, the baseline run was repeated with every parameter unchanged except the kernel centre, which was moved 9 m south from (100.5, 36.5, 6.8) to (100.5, 27.5, 6.8) — inside the corridor strip, at the position suggested by the drone imagery. The qualitative pattern is unchanged: damage remains concentrated on the south side, the roof is breached directly above the ignition point (11 roof tiles versus 10), a single slab tile fails, and the corridor doors fail within the first venting legs (the first tens of milliseconds). The south-first sequence becomes even more pronounced: the facade panel directly outside the kernel now fails at the first sampled instant (0.02 s, rather than 0.04 s). The aerial comparison in Fig. 2(g–l) shows the same signature: the corridor run vents along the south facade from the first frames, and at 2–4 s its dust plume remains concentrated toward the south edge, with weaker northward spill than the central-ignition baseline. Totals shift downward — 60 of 255 panels fail, versus 79 — because with the kernel adjacent to the south wall the earliest vent openings form immediately in the closest facade panels and bleed the interior sooner; north-facade failures drop from 16 to 9. The sustained overpressure at the tenant-zone reference probe rises from 2.2 to 3.1 kPa — with edge ignition, the burn reaches the cloud centre later, extending pressure production into the 0.05–0.30 s averaging window — but remains of the same few-kilopascal order. The second-storey stripping band on the south facade is identical in the two runs (a contiguous 60 m from x = 70 to 130 m), whereas ground-storey stripping shrinks, so the both-storey contiguous measure used in Table 5 drops from 60 m to 30 m. Under the no-tuning principle of Section 4.2, both results are reported as computed: the corridor ignition matches the newly reported epicentre position and preserves the upper-storey stripping band and roof breach, while the baseline central-aisle ignition reproduces the observed both-storey stripping extent more closely. The headline conclusions — south-side concentration, a roof breach above the epicentre, and interior loads of a few kilopascals acting on seismically weakened members — do not hinge on the exact ignition location.

Contiguous facade stripping is measured throughout this paper as the longest run of adjacent 10 m facade slots in which *both* facade layers (fs1 and fs2) have failed, which corresponds to the “stripped to the frame” condition identified in the aerial record; the same definition is applied to both grids. A single-layer criterion (fs2 only), used in an earlier draft of this work, gives 50 m on the baseline grid. Readers comparing with that earlier figure should note the change in definition rather than a change in result.

Table 4. Simulated failure sequence (1.0 m baseline grid).

Time	Simulated event
0.02 s	Kernel pressure pulse (+34 kPa locally): roof tile above and slab tile below ignition fail; nearest demising wall fails
0.04–0.12 s	South facade ALC begins stripping (+3.5–6.9 kPa); 1F glazing; north facade follows; partition band destroyed
0.1–0.5 s	Main burn: 2.7–4.6 kPa sustained in the zone; 60 m contiguous facade loss; 10 roof tiles; external blast at +2.9 kPa
0.35–0.7	Storey-crush core: 9 columns fail first; bays above pancake to rubble

Time	Simulated event
s	heights of 1–2.2 m
0.5–3 s	Peripheral slab unzipping (48 tiles with durations of 0.35–0.65 s per tile); columns losing all slab support topple; roof follows down
~1.5 s	Combustion complete; 79/255 panels fail under direct gas pressure

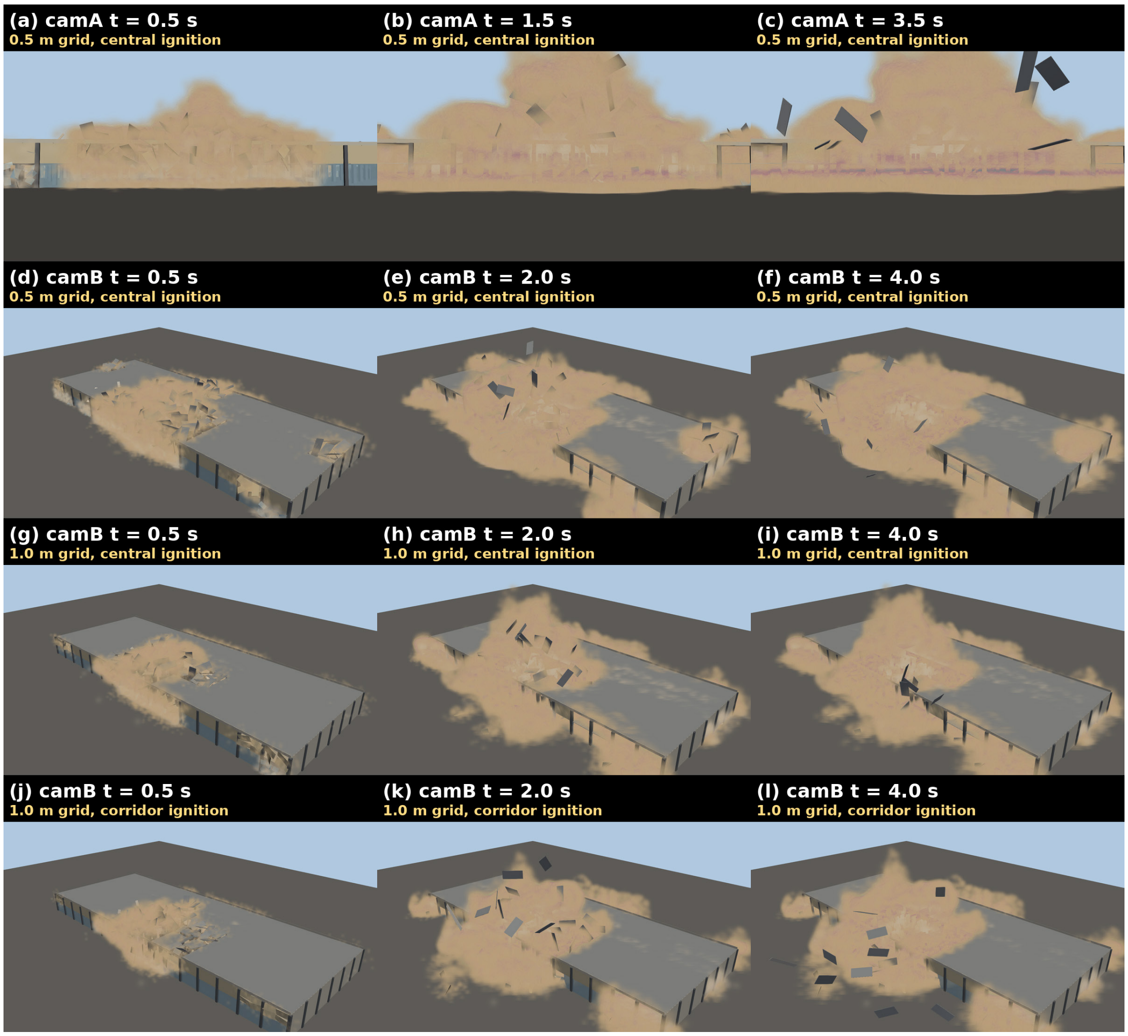

Figure 2. Simulation frames. (a–c) Road-level view corresponding to the dashcam angle at t = 0.5, 1.5, and 3.5 s, and (d–f) aerial view at t = 0.5, 2.0, and 4.0 s, both from the refined 0.5 m central-ignition run; (g–i) the 1.0 m central-ignition baseline and (j–l) the 1.0 m corridor-ignition sensitivity run of Section 4.1, aerial views at the same instants. Comparing (g–i) with (j–l) isolates the effect of ignition location on the same grid: the corridor run vents along the south facade from the outset (j), whereas the central run ejects more material through the roof breach in the first half-second (g); at 2–4 s, the corridor plume remains concentrated toward the south edge, with visibly weaker

northward spill (k, l versus h, i), consistent with the failure counts in Section 4.1, while the roof breach above the ignition point and the crushed core develop similarly in both runs. Tan particles: structural dust; grey boxes: panel fragments. The crushed core with stacked floor/roof plates is discernible in (f) through the dust. The refined run resolves the vent jets and the debris release more finely, and its panel-failure counts are those in Table 6; those of the two 1.0 m runs are given in Table 4 and Section 4.1. All frames are renderings of the present simulation; no broadcast imagery is reproduced in this paper.

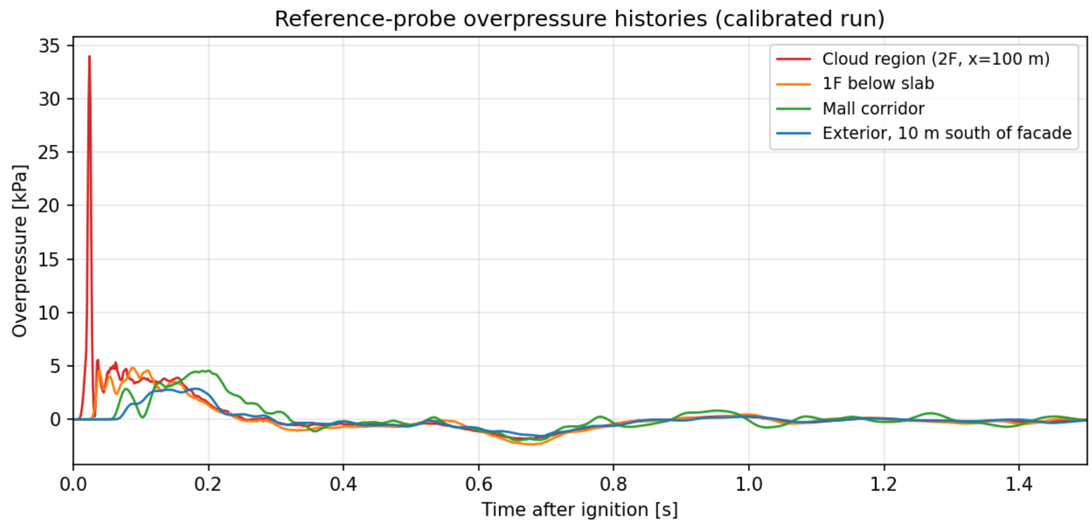

Figure 3. Overpressure histories at reference probes at the cloud centre, first floor (1F), corridor, and exterior.

4.2 Comparison with observations

Table 5 compares the footage-derived reconstruction targets of Table 1 with the simulation. The “role” column is essential to interpreting this table: the first two rows were used to select the burning velocity in Section 3.2 and therefore cannot be counted as validations, whereas the remaining rows were not used in any calibration.

Table 5. Reconstruction targets versus simulation, with the role of each quantity in the study. Ballistic quantities were never used in calibration.

Quantity	Observed	Simulated	Role
Contiguous facade stripping	~55 m (±15 m)	60 m (both grids)	**calibration target**
Near-frame-one envelope failure	~27 m wide eruption at 33 ms	envelope failure in time range 0.02–0.04 s over tens of metres	**calibration target**

Quantity	Observed	Simulated	Role
Total facade damage span	~95 m	scattered failures to ~150 m (over-predicted fringe)	independent
Rear (tank-side) damage	radial sheet scatter	9–11 north-facade panels ✓	independent
Roof damage zone	local breach 10–15 m	tiles clustered above cloud (same zone; count grid-sensitive)	independent
Collapse morphology	~7 bays; crushed core + draped plates	crush core ~20 × 20 m + unzipping band; footprint ~50 × 40 m ✓	independent
External fireball	no sustained fireball (brief vent flashes)	none sustained — transient vent flames are below grid resolution	independent
Initial dust-front speed	13 m/s (band 8–17)	8.8 m/s (1.0 m); 7.6 m/s (0.5 m)	independent — within band on the baseline grid, marginally below on the refined grid
Late front speed	4 m/s (3–7)	~2 m/s (under-predicted after CFD record ends)	independent
Roof-debris launch speed and apex	30–40 m/s; apex ~24 m (band 15–33 m)	sheets (6.3 kg m^{-2}): v_z median 21.0 m/s (IQR 15.6–29.5, P90 43.6), apex median 21.6 m (IQR 18.5–32.6), n = 200; tiles (50 kg m^{-2}): 9.4 m/s, apex 18.0 m, n = 60	independent — apex ✓, launch speed partially
Debris throw	steel sheeting to ~100 m (lower bound)	sheets P95 8.7 m, max 20.2 m (n = 200)	independent — **not reproduced** (see text)

The last two rows constitute the most demanding independent test in this study, and the outcome is mixed and instructive. The observed launch speed and apex height are not independent observables: for thin steel skin of areal density ~6.3 kg m^{-2}, quadratic drag limits the still-air rise to 11–13 m for launch speeds of 30–40 m/s, so the observed pair (30–40 m/s and apex ≈ 24 m above ground from an 11 m roof) jointly constrains the release impulse and the drag treatment (Fig. 7b). Applying the unchanged 25 ms impulse law of Section 3.4 to sheeting of that areal density at the recorded roof-tile failure pressures ($\Delta p \approx 5.6$–24 kPa with median ≈ 10 kPa) yields apex heights with an interquartile range (IQR) of 18.5–32.6 m, which covers the observed band well, and launch speeds whose IQR is 15.6–29.5 m/s with P90 = 43.6 m/s, so that the observed 30–40 m/s band corresponds to roughly the 75th to 90th percentile of the simulated sheet population rather than to its centre. The agreement in apex is therefore stronger than the agreement in launch speed. The CFD vent jets lift part of the population above the still-air curves, and the heavier lumped tiles reach the same apex band at proportionally lower launch speeds, as the analytic curves in Fig. 7b make explicit.

A closed-form check makes the significance of this test explicit. The impulse law is inverted for the observed pair to obtain $\tau = v0\ \mu / \Delta p \approx 35 \times 6.3 / 10{,}000 \approx 22$ ms. Compared with the 25 ms assumed a priori in Table 3, this is a 12% agreement obtained from an observable that played no part in setting the parameter.

The throw distance is **not** reproduced: simulated sheets land within 20 m of the building (P95 = 8.7 m) against an observed lower bound of ~100 m. Vertically launched roof debris cannot traverse such distances under quadratic drag. The long-range sheeting in the aerial record most plausibly originated as near-horizontally launched facade skin or roof-edge flashing carried by the lateral vent jets — a debris class that the ALC-typified facade panels of this model do not represent. This deficiency is deliberately reported as a finding rather than removed by adjustment so that the ballistic observables remain an independent test.

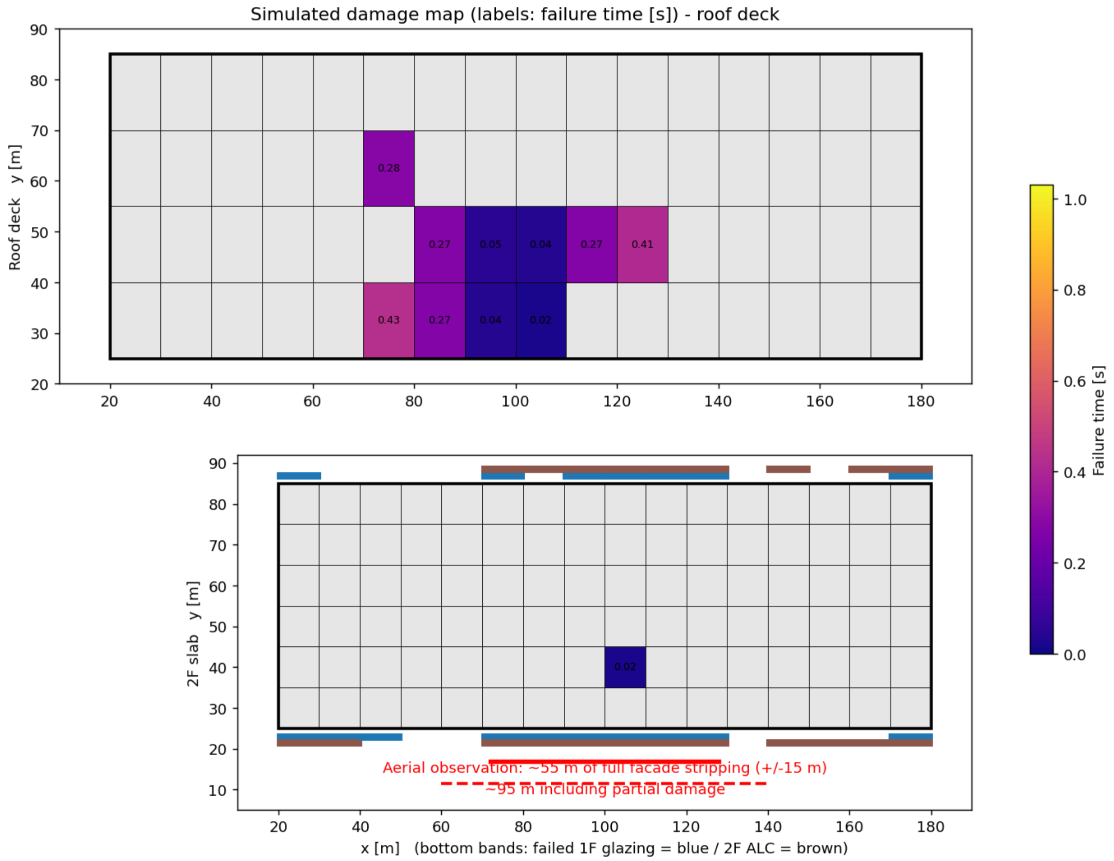

Figure 4. Simulated damage map (failure times) for the roof deck (top) and second-floor (2F) slab with facade bands (bottom), compared with the aerially observed facade-stripping extents (red lines). The extents are transcribed from public aerial footage, and no imagery is reproduced.

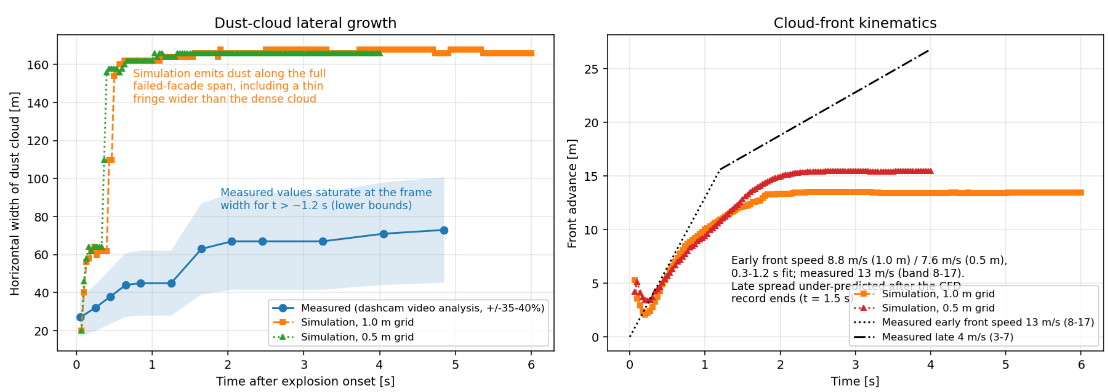

Figure 5. Dust-cloud kinematics versus dashcam measurements: lateral growth (left) and front advance (right), shown for both grids. The front speeds quoted in the text and in Tables 5 and 6 — 8.8 m/s on the 1.0 m grid and 7.6 m/s on the 0.5 m grid — are linear

fits over 0.3–1.2 s. The measured value is 13 m/s with an 8–17 m/s scale-uncertainty band.

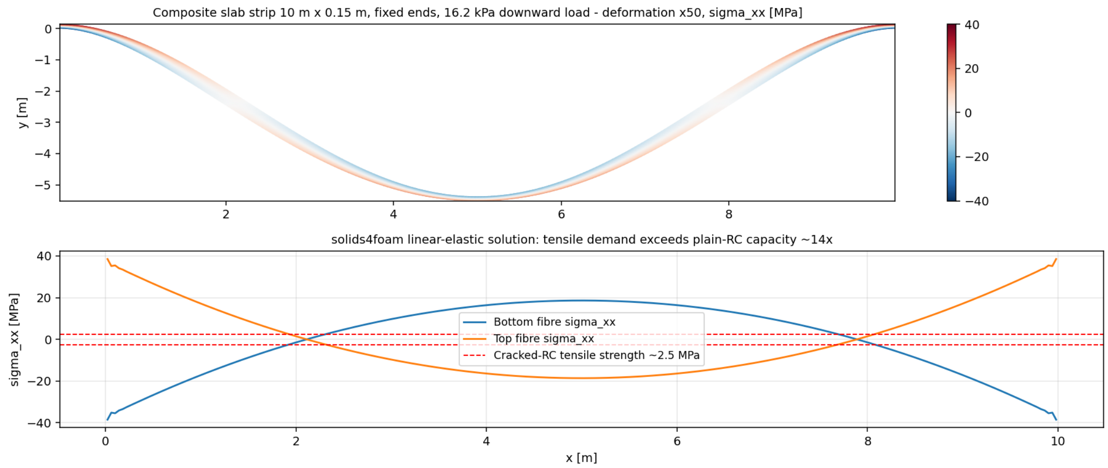

Figure 6. Independent solids4foam check of the slab failure criterion.

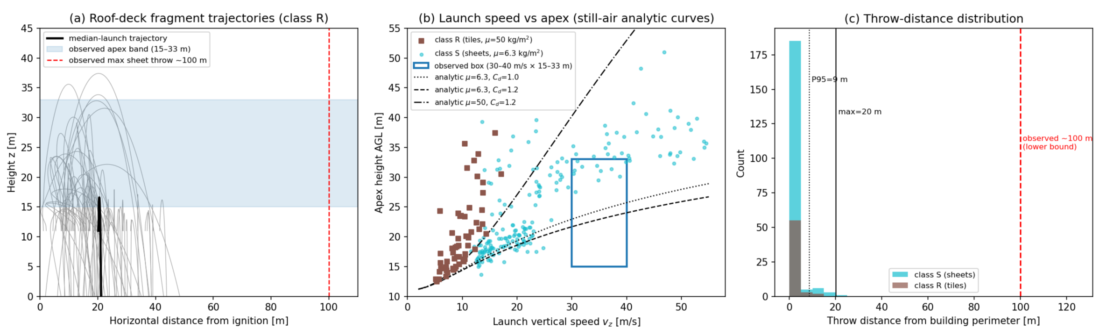

Figure 7. Independent test of the debris model against public-footage ballistics. (a) Simulated trajectories of roof-deck fragments, where the shaded band represents the observed apex with video-scale uncertainty, and the dashed line the observed maximum sheet-metal throw. (b) Launch vertical speed versus apex height for both fragment classes, with the observed box and the analytic quadratic-drag relations for areal densities of 6.3 kg m^{-2} (two drag coefficients) and 50 kg m^{-2}; points above the still-air curves are lifted by the CFD vent jets. (c) Throw-distance distributions, where the observed ~100 m is a lower bound set by the debris identifiable in the footage and is not reproduced by roof-normal launches (see the main text). None of these quantities were used in any calibration.

4.3 Grid sensitivity

The reconstruction was repeated on a uniformly refined 0.5 m mesh (4.56 M fluid cells and the time step halved to 0.125 ms) with all other settings — the prescribed wrinkling factor, the panel capacities of Table 2, the degradation factor, the cloud definition, and the ignition kernel — kept identical. The propane inventory integrates to 325.5 and 331.0 kg on the two grids (a 1.7% lattice-snapping difference), and the deterministic mesh-rebuild machinery reproduces cell centres to within 8.5e−14 m on the fine grid. The 0.5 m spacing preserves the 10 m panel lattice exactly and resolves the 1 m merchandising obstacles with two cells rather than one.

Because the wrinkling factor is prescribed rather than emergent, the burning rate is by construction largely independent of the mesh. This test therefore isolates the discretization of the pressure field, the venting flow, and the geometry, which is precisely the part of the chain on which the damage-extent conclusions depend.

Table 6 and Fig. 8 summarize the comparison. The outcome should be interpreted as partial rather than complete convergence. Near-field and impulsive quantities behave as expected for a marginally resolved ignition kernel and single- or double-cell vent jets: the kernel peak decreases by 17%, the external blast spike at the road probe more than doubles, and the tiles that fail because of kernel-driven jets rise from 10 to 17 (roof) and from 1 to 6 (slab), carrying the total panels failing under direct pressure from 79 to 100, an increase of 27%. **The 1-m-mesh results are therefore not convergent for local peaks or for near-kernel failure counts, and are not conservative with respect to the latter.** Two quantities that carry the conclusions of this paper are, by contrast, essentially unchanged: the contiguous facade-stripping length is 60 m on both grids, and the sustained tenant-strip overpressure changes by 8%. The initial dust-front speed changes by 14%, from 8.8 m/s to 7.6 m/s. The baseline value lies inside the observed 8–17 m/s band while the refined value falls marginally below its lower bound, so the cloud kinematics are reproduced at the order-of-magnitude level on both grids but are not themselves grid-convergent. The overall reading is that the *extent* of the damage and the gross cloud kinematics survive a halving of the cell size, whereas absolute local pressures and failure counts do not. The latter are reported here rather than suppressed, and any use of the present overpressures as design quantities would be unwarranted.

Table 6. Grid-sensitivity metrics. The conclusions of this paper rest on the facade-stripping length, the sustained compartment overpressure, and the dust-front speed (bolded rows).

Metric	1.0 m	0.5 m	Δ
Cells/maximum time step	0.57 M/0.25 ms	4.56 M/0.125 ms	—
Peak overpressure, ignition-kernel probe	34.0 kPa	28.4 kPa	−17%
Sustained overpressure, tenant strip (0.05–0.30 s mean)	**2.24 kPa**	**2.43 kPa**	**+8%**
External blast peak, road probe	2.87 kPa	6.16 kPa	+114%
Panels failed under direct pressure (out of	79	100	+27%

Metric	1.0 m	0.5 m	Δ
255)			
Contiguous facade stripping length	**60 m**	**60 m**	**0**
Roof tiles failed	10	17	+7 tiles
Slab tiles failed	1	6	+5 tiles
Cloud-centre decay below 1 kPa	0.213 s	0.195 s	−8%
Initial dust-front speed (0.3–1.2 s fit)	**8.8 m/s**	**7.6 m/s**	**−14%**
Maximum cell-centre displacement across rebuilds	< 1e−13 m	8.5e−14 m	—

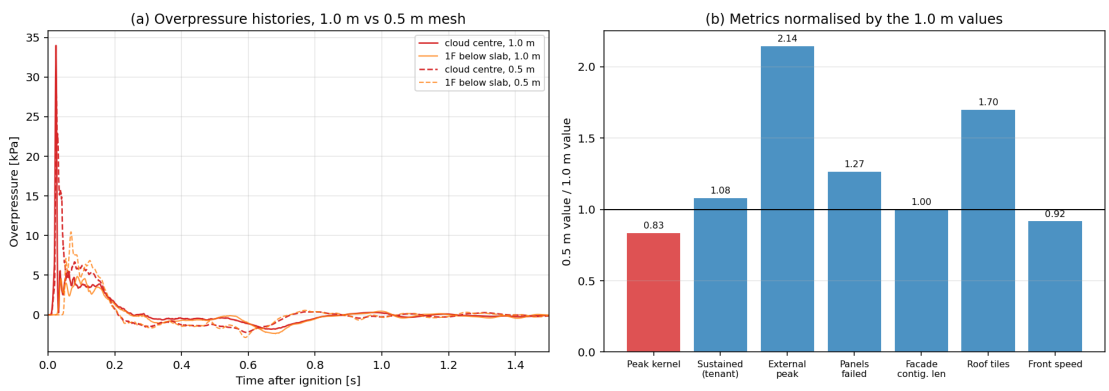

Figure 8. Grid sensitivity. (a) Overpressure histories at the cloud-centre and 1F probes for the 1.0 m (solid) and 0.5 m (dashed) meshes. (b) Integrated metrics normalized by their 1.0 m values. The near-kernel transient and the external blast spike are strongly grid-dependent, as expected for a 2.5 m ignition kernel and single- or double-cell vent jets; the facade-stripping length and the sustained compartment overpressure are not.

5. Discussion

Calibration and its meaning. With realistic momentum dynamics and venting, uncalibrated RANS burning (with initial cloud turbulence $u' \approx 0.8$–2 m/s) produced only ~1–2 kPa, which is sufficient for partitions and little else, but incompatible with the observed damage. Reproducing the evidence required congested-space burning velocities at the upper end of the reported range together with damage-class-III seismic degradation (0.45) of member capacities. Read inversely, the observed damage pattern itself constrains the event physics: either the effective burning velocity reached the top of the congested-space range (strong obstacle-driven acceleration, possibly aided by ceiling-plenum channelling that our geometry omits), or member capacities after intensity-7 shaking were substantially below intact values, or (most plausibly) both. This coupling of Natech pre-damage with explosion loading is, we believe, the principal engineering lesson: post-earthquake gas safety assessments should not assume intact structural resistance when judging acceptable leak and ignition risk. Should the official investigation establish that gas isolation did not occur as intended, the reliability of seismic shutoff provisions for bulk LP installations serving large public buildings would warrant review. That determination, however, is beyond the scope of this study.

What the ballistic test does and does not establish. The debris comparison in Section 4.2 is the only place in this work where a prescribed parameter in Table 3 is confronted with an observable it did not play a part in setting. The apex heights agree, and the impulse duration back-calculated from the observed pair (22 ms) agrees with the assumed value (25 ms) to 12%. The launch-speed distribution is centred lower than the observed band, and the throw distance fails outright. The failure is informative: it localizes a missing debris class — near-horizontally launched thin skin — rather than casting doubt on the impulse law itself, and it identifies the most valuable single extension of the model.

Overpressure in context. For scale context only, the town-gas explosion at Ronan Point [9] is commonly associated with internal overpressures of approximately 20 kPa. The broad 3–5 kPa sustained in the present reconstruction, with a 34 kPa local kernel transient on the baseline grid, is of the same order of magnitude. The comparison should not be read as validation: the enclosure volume, venting area, fuel, and structural systems all differ substantially; no overpressure was measured in the present event; and Section 4.3 shows that the local peak itself is grid-dependent.

Deflagration or detonation? The combustion regime of this event has been debated publicly, and the present work bears on that question asymmetrically. It does not test the detonation hypothesis: the solver is a deflagration model with a prescribed turbulent burning velocity and contains no deflagration-to-detonation-transition (DDT) mechanism, and the 1.0 m and 0.5 m meshes are orders of magnitude too coarse to resolve one. What the reconstruction establishes is sufficiency: a fast, congestion-driven deflagration at the upper end of the reported burning-velocity range, acting on seismically degraded members, reproduces the observed damage extent, the mixed crush/draped collapse morphology, the dust-front kinematics, and the absence of a sustained fireball without invoking detonation-level loads. The brief flame luminosity at the cloud base in the close-range recording aired on 3 August [15], interpreted in Section 2.2 as transient vent-jet flames, is itself a classic signature of a vented deflagration (the external combustion of vented unburned mixture), and the expert assessment that rooftop units were lifted “by pressure from below” [15] is likewise consistent with sustained quasi-static internal pressure rather than with a propagating shock.

Conversely, a fully developed Chapman–Jouguet (CJ) detonation of the cloud can be excluded on damage-magnitude grounds. For near-stoichiometric propane–air, the CJ pressure is approximately 1.9 MPa and normally reflected pressures are approximately 2.5 times larger [16]. Against the connection-governed capacities of Table 2 — 12.2–27 kPa for the composite slab tiles and 2.7–6 kPa for the ALC facade — the static excess is two orders of magnitude. The natural objection, that detonation loading is impulsive and should be judged on impulse rather than peak pressure, does not change the conclusion. Taking the post-Taylor-wave average of 0.5 MPa over a 10–30 ms positive phase yields a surface impulse of roughly 5–15 kPa·s. The corresponding figure obtained from the reflected peak and a triangular decay is three to five times higher, so the estimate used here is deliberately conservative. For floor plates with a fundamental period of order 0.1–0.3 s, the impulsive asymptote of the pressure–impulse curve corresponding to a 12–27 kPa static resistance is of order 1–3 kPa·s [17]; the detonation demand therefore exceeds the tabulated capacities by a factor of several to more than an order of magnitude, depending on which end of each range is taken. Nor can the building's exceptional venting reconcile a detonation with the observations: venting caps the pressure of a deflagration because the burn (of order 1 s) is slow compared with the response of the 255 failing panels, whereas a detonation would traverse the 50 m cloud in approximately 28 ms, outrunning vent formation entirely, so the structure would receive near-CJ loading regardless of how well the envelope vented. Such loading would leave neither standing columns nor floor plates draped between them.

The debris ballistics of Section 4.2 provide a direct, observational bound on the load actually delivered. The sheet debris tracked in the footage (with areal density ~6.3 kg m^{-2}) was launched at 30–40 m/s, corresponding to a surface impulse of only ~0.2 kPa·s — consistent with the ~22 ms deflagration impulse inferred independently in Section 4.2. The detonation-scale impulse estimated above would impart velocities of order 10^3 m/s to the same sheeting — a loading at which the skin would tear and fragment rather than accelerate coherently. That the aerial record instead shows intact sheets following gravity-consistent parabolas at a few tens of metres per second is, by itself, incompatible with detonation loading of the surfaces that released them. The same reasoning disposes of the argument that the frame-to-frame simultaneity of envelope failure implies supersonic propagation: as noted in Section 2.2, pressure equalizes on the acoustic timescale (11 m per video frame), so panels tens of metres apart can fail within one frame under a subsonic deflagration — and the debris they shed in that same frame moves at deflagration, not detonation, speeds.

The strongest structural indication is indirect. Reproducing the observed damage required both the upper-bound burning velocity and the damage-class-III capacity reduction of 0.45; with intact member capacities the same combustion produced markedly less damage. A detonation would have required no capacity reduction at all. Th at the observed damage is explicable only for members already weakened by the mainshock is itself evidence that the loading was not of detonation order — and it is precisely this coupling that gives the event its Natech character. The vehicle damage reported in the public record (Table 1) is consistent with the same picture: a single truck driving past the mall was wrecked [15], an outcome that an external blast of a few kPa accompanied by sheet and glass debris can readily cause, while multiple dashcams in the nearby queue recorded continuously — a record that a detonation-scale external blast at tens of metres would not have left intact.

Two caveats are necessary. First, the calibrated burning velocity sits at the top of the 4–20 m/s range reported for highly congested spaces, so the inferred regime is a fast deflagration rather than a slow one, and regimes in which a DDT becomes conceivable are not far above it. Second, a transient, localized transition to detonation within a particularly congested sub-region, decaying on leaving it, cannot be excluded by this work. Mixture detonability confines where such a transition could have occurred: the detonation cell size of propane–air is of order 5 cm near stoichiometry and grows steeply on the lean side [16], so the lean ceiling layer (ft = 0.030 with an equivalence ratio of approximately 0.48) lies outside the reported lean detonability limit of propane–air, which sits near an equivalence ratio of 0.7 depending on configuration, and is effectively non-detonable. The intermediate layer (0.74) is marginal, and only the near-stoichiometric floor layer within the congested racking is a plausible host. Addressing that possibility would require sub-centimetre resolution and detailed chemical analysis. The unmodelled ceiling plenum remains the most plausible run-up path to examine first, with the same detonability caveat applying to its leaner mixture.

Collapse morphology. The two observed morphologies are a crushed core that "lost its original form" and surrounding bays with plates draped between standing columns. These morphologies emerge naturally from the two implemented mechanisms (column-first crush versus slab-first unzipping), supporting the interpretation that near-field blast impulse on quake-damaged columns initiated a storey collapse. At the same time, the wider floor loss propagated as a gravity-driven cascade of connection unzipping. It should be borne in mind that the timing parameters of both mechanisms are prescribed (Table 3), so the agreement concerns the morphology rather than the collapse kinetics.

Limitations. The limitations of this study are as follows. Geometry is typified from public information (without drawings); the ceiling plenum, HVAC, fire compartmentation, and real merchandising are absent; the cloud mass and extent are a hypothesis consistent with, but not proven by, public data; S_T is prescribed rather than emergent, and the facade-stripping extent used to select it is consequently not an independent check; the collapse-stage parameters of Table 3 are likewise prescribed, with the exception of the impulse duration tested in Section 4.2; slab "opening" in the CFD approximates collapse venting; the collapse dynamics are one-way (no back-coupling of collapsing plates on the gas); the model contains no near-horizontally launched thin-skin debris class and consequently under-predicts long-range throwing by an order of magnitude; absolute video scales carry ±35–40% uncertainty, and measured cloud widths beyond ~1.2 s are frame-limited lower bounds; and the mesh under-resolves local blast interactions near the ignition kernel and the vent jets, as quantified by the 0.5-m-mesh comparison of Section 4.3 (the local peaks are at −17% and +114%, and near-kernel failure counts are +27%). Convergence was assessed on two grids only, and no Richardson extrapolation or grid-convergence index is claimed. None of these affects the qualitative sequence, but quantitative local overpressures should be interpreted as order-of-magnitude estimates. The solver contains no DDT mechanism, and the question of a localized DDT is outside the scope of the present grids and chemistry (as discussed in the subsection “Deflagration or detonation?” in Section 5).

6. Conclusions

An open-source, three-stage FSI reconstruction of the 2026 Kumamoto mall explosion was calibrated on a single gas-dynamic parameter, and fixed using the observed facade-stripping extent and the near-frame-one envelope failure. With that calibration in place, the model independently reproduces the absence of a sustained external fireball, the radial debris scatter on the rear facade, the localized roof breach, the mixed pancake/draped partial collapse of the second floor, and a dust-front speed of 8.8 m/s against a measured 13 m/s within a band of 8–17 m/s. This is done using a stratified propane cloud with a mass of approximately 330 kg, congested-space burning velocities ($S_T \approx$ 8–20 m/s across the stratified layers), and damage-class-III seismically degraded member capacities.

The debris model was tested—not calibrated—against the ballistics recorded in the footage. It reproduces the observed apex band, and the back-calculated impulse duration of 22 ms agrees to within 12% with the 25 ms assumed a priori. It does not reproduce the longest observed throws, which implies a missing class of near-horizontally launched thin skin and is reported as a finding rather than removed by adjustment.

A uniform mesh refinement to 0.5 m leaves the contiguous facade-stripping length unchanged and the sustained compartment overpressure within 8%, while the near-kernel peak, the external blast spike, and the local failure counts change by tens of percent and are not convergent. The damage-extent conclusions therefore survive refinement whereas the absolute local pressures do not, and the latter should not be used as design quantities.

On the grounds of damage magnitude, impulse, and debris velocity, the reconstruction supports a fast, congestion-driven deflagration rather than a cloud detonation. The present grids and chemistry cannot exclude a transient, localized transition confined to the near-stoichiometric floor layer.

The staged panel-venting scheme (consisting of deterministic mesh-rebuild restarts) provides a practical route to pressure–failure feedback in explosion CFD without moving-mesh machinery, and the documented subsetMesh empty-patch pitfall is of immediate practical value to OpenFOAM users. The results are consistent with a Natech interpretation in which earthquake pre-damage of both the gas supply system and the structure contributed to the severity of the outcome. Whether that interpretation is correct, and what regulatory consequences follow from it, rest with the official investigations.

Ethics and disclaimer

This reconstruction is based exclusively on publicly available information (broadcast footage, operator and government releases) and typified engineering data. It does not use, nor did its authors have access to, any non-public investigation material. No broadcast or third-party imagery is reproduced in this paper. All figures are the authors' own renderings and plots, and quantities derived from footage are reported as measurements only. All quantitative findings are engineering hypotheses intended to support scientific discussion; determining the cause of the accident rests with the official investigations (fire service, METI, police). No attribution of legal responsibility is made or implied. Casualty figures cited reflect public reporting as of 30 July 2026 and may be revised. The authors express their condolences to the victims and their families.

Use of AI tools

In accordance with the engrXiv AI policy, the authors disclose the following use of AI/LLM tools in preparing this work: assistance with English language editing and document preparation of author-written text, assistance in identifying candidate publication venues, critical review of author-written drafts leading to revisions of framing and presentation, and assistance in specifying the design and reporting format of the independent verification tests presented in Sections 4.2 and 4.3. All numerical models, the simulation set-up, the video measurements, the execution of all simulations and analyses, the results, the verification cases, and the scientific interpretation were produced and checked by the authors. No text was accepted verbatim without author review, AI tools generated no data or figures, and no AI system is listed as an author.

Data and code availability

The complete case-generation scripts, staged-venting driver, collapse and dust dynamics code, minimal reproductions of the subsetMesh pitfall, and rendered animations are available from the corresponding author. They are intended for deposit in a public repository alongside this preprint, together with the 0.5 m grid-sensitivity case, the per-fragment ballistic trajectories (fragments_roof.csv, fragments_sheet.csv, ballistics_raw.json), and the extraction and plotting scripts. Fragment and particle counts quoted in Section 3.4 refer to the archived production run.

Acknowledgements

The simulations were performed on a workstation at the Institute of Fluid Science, Tohoku University. Part of the numerical results in this research were obtained using supercomputing resources at the Cyberscience Center, Tohoku University. The numerical simulations were partially performed using FUJITSU AFI-NITY scalar parallel computers at the Institute of Fluid Science, Tohoku University. No external funding was received for this study. Mark R. Kurban from Edanz (https://www.jp.edanz.com/ac) edited a draft of this manuscript.

References

[1] Weller HG, Tabor G, Gosman AD, Fureby C. Application of a flame-wrinkling LES combustion model to a turbulent mixing layer. Proc Combust Inst. 1998;27:899–907. DOI: 10.1016/S0082-0784(98)80487-6

[2] Gülder ÖL. Correlations of laminar combustion data for alternative S.I. engine fuels. SAE Technical Paper 841000; 1984. DOI: 10.4271/841000

[3] Menter FR. Two-equation eddy-viscosity turbulence models for engineering applications. AIAA J. 1994;32(8):1598–1605. DOI: 10.2514/3.12149

[4] OpenCFD Ltd. OpenFOAM-v2606 User Guide; 2026. Available at https://www.openfoam.com; User Guide (PDF): https://dl.openfoam.com/source/v2606/UserGuide.pdf

[5] Harris RJ. The Investigation and Control of Gas Explosions in Buildings and Heating Plant. E & FN Spon; 1983. Record: Google Books

[6] Bauwens CR, Chaffee J, Dorofeev S. Effect of ignition location, vent size, and obstacles on vented explosion overpressures in propane–air mixtures. Combust Sci Technol. 2010;182(11–12):1915–1932. DOI: 10.1080/00102202.2010.497415

[7] NFPA 68. Standard on Explosion Protection by Deflagration Venting. National Fire Protection Association; 2018. Record: NFPA LiNK (2018 edition)

[8] EN 1991-1-7:2006. Eurocode 1: Actions on structures — Part 1-7: General actions — Accidental actions. CEN; 2006. Record: European Commission JRC

[9] Griffiths H, Pugsley A, Saunders O. Report of the Inquiry into the Collapse of Flats at Ronan Point, Canning Town. HMSO; 1968. Record: Google Books

[10] Architectural Institute of Japan. Design Recommendations for Composite Constructions. AIJ; 2010 (in Japanese). Record: NDL Search

[11] Japan Building Disaster Prevention Association. Standard for Damage Level Classification and Guidelines for Restoration Techniques of Earthquake-Damaged Buildings. JBDPA; 2015 (in Japanese). Record: JBDPA publication page

[12] Cardiff P, Karač A, De Jaeger P, Jasak H, Nagy J, Ivanković A, Tuković Ž. An open-source finite volume toolbox for solid mechanics and fluid–solid interaction simulations. arXiv:1808.10736; 2018. DOI: 10.48550/arXiv.1808.10736

[13] Hansen OR, Hinze P, Engel D, Davis S. Using computational fluid dynamics (CFD) for blast wave predictions. J Loss Prev Process Ind. 2010;23(6):885–906. DOI: 10.1016/j.jlp.2010.07.005

[14] Japan Meteorological Agency. Information on the earthquake of 28 July 2026 in Kumamoto Prefecture (Mj 7.1, maximum seismic intensity 7). JMA press releases; July 2026 (in Japanese). Record: JMA event record

[15] Operator and broadcast sources on the 28 July 2026 mall explosion: AEON Co., Ltd. press release (29 July 2026); NHK, NTV/news zero, FNN and KAB broadcasts (28–30 July 2026), including dashcam and aerial footage; dashcam footage provided to the Mainichi Shimbun (published 30 July 2026); and the NTV “Shinso Hodo Bankisha!” documentary (aired 3 August 2026), including drone surveys of the site, employee interviews, and a close-range recording of the explosion (in Japanese). Records: AEON news archive.

[16] Kaneshige M, Shepherd JE. Detonation database. GALCIT Report FM97-8, California Institute of Technology; 1997 (with updates). Record: Caltech Detonation Database

[17] US Department of Defense. Structures to Resist the Effects of Accidental Explosions. UFC 3-340-02; 2008. Record: WBDG Unified Facilities Criteria